International Journal of
Turbomachinery
Propulsion and Power

MDPI

Article

Optimising Blade Profiles to Extend the Operating Range in BLI Fan Application †

Andrea Magrini * and Ernesto Benini

Department of Industrial Engineering, University of Padova, via Venezia, 1, 35131 Padova, Italy; ernesto.benini@unipd.it

* Correspondence: andrea.magrini@unipd.it

† This paper is an extended version of our paper published in Proceedings of the 16th European Turbomachinery Conference, Hannover, Germany, 24–28 March 2025.

Abstract

Boundary Layer Ingestion propulsors operate in an adverse aerodynamic environment with high levels of distortion. With the purpose of extending the operating range of transonic fan rotors for BLI applications, in this paper we present an optimisation study focused on blade profiles design under different working conditions. Quasi-2D blade sections are optimised using a genetic algorithm and numerical simulations, by varying the camberline and thickness distribution. A method to efficiently achieve a combination of total pressure ratio at a given relative inlet Mach number is devised. The isentropic efficiency is optimised at the design point, concurrently with the stall total pressure ratio at a lower inlet Mach number, in a multi-objective fashion. Pareto-optimal profiles exhibit a moderate leading edge concavity for high efficiency and a straighter fore part with increased trailing edge deflection for higher compression at stall. Optimised airfoils are used in a preliminary three-dimensional evaluation with a realistic BLI inflow, in which the unsteady full-annulus analysis corroborates the approach of the sectional optimisation, also showing the possibility of estimating the integral performance of the machine with a simplified approach based on a single-passage simulation with a circumferential-averaged inflow distribution.

Keywords: transonic fan; boundary layer ingestion; turbomachinery optimisation; inlet distortion

1. Introduction

The need to develop novel aeroengine designs able to operate under increased distorted conditions stems from the growing importance of tightly integrated powerplant configurations in civil aviation, tending to submerged propulsors layout in Boundary Layer Ingestion (BLI) propulsion [1]. Boundary layer energisation has been long recognised to offer theoretical propulsive benefits, as it allows to reduce the kinetic energy waste at the jet by producing thrust through accelerating a fluid moving slower than the airplane [2,3], thus overcoming the well-known Froude lemma for an isolated propulsor showing the need of an overspeed at the nozzle to produce a propelling force.

The research in BLI propulsion has noticeably grown in the last twenty years, with plenty of studies facing suitable bookkeeping methods based on near-field, far-field, or energy approaches to characterise and quantify the effects of BLI on a fluid-dynamics basis [4], and many other focused on the more detailed evaluation of aircraft configurations with partly submerged engines in different installations.

Received: 20 August 2025
Revised: 5 December 2025
Accepted: 26 February 2026
Published: 6 April 2026

For instance, Seitz et al. [5] reported the CENTRELINE project design efforts for a propulsive fuselage configuration, reaching around 5% mission fuel burn benefit using optimised aero-shaping. Bravo-Mosquera et al. [6] designed and tested a conventional and a BLI aircraft, proving reduced electric power and kinetic energy waste for the latter. Uranga et al. [7] tested the D8 double bubble aircraft with 40% of the fuselage boundary layer ingested, measuring a propulsor mechanical power reduction of 9%, in agreement with theoretical methods. Lee [8] correlated BLI wake characteristics to power savings and fan performance using CFD experiments.

In addition to these aircraft design studies, some authors have inevitably faced the gist of the BLI technology, that is, the possibility of realising in practice the boundary layer energisation by means of a fluid machinery. In fact, the major challenge for developing BLI vehicles is to design fan rotors that can efficiently and stably operate within the distorted inflow conditions resulting from the complex coupling between the fuselage flow and the superimposed rotor effect. Several authors have investigated via experimental and numerical tests the impact of flow distortion on low-pressure ratio fans.

Gunn et al. [9] experimentally investigated the aerodynamics of a low-speed rotor under a BLI distortion, identifying key flow features. Perovic et al. [10] expanded the study to stall inception mechanisms, showing the ability of the rotating blades to recover periodically from post-critical conditions in steady passage flow. Lee and Liou [11] conducted an optimisation for a fan with outlet guide vanes (OGV) in a tail cone thruster, using CFD simulations of the installed stage at cruise. Battiston et al. [12] carried out a three-dimensional fuselage and nacelle optimisation for an aft-fuselage BLI propulsor and the fan engine design to operate under the BLI conditions. Castillo-Pardo et al. [13] presented two rotor designs for the propulsive fuselage concept, showing that an adaptation of the typical blade stagger to the BLI conditions can enhance the performance. The fan was tested experimentally with different sideslip directions by the same author, who stressed the importance of swirl distortion in addition to total pressure for BLI application [14]. The fan was simulated under installation with unsteady Reynolds-Averaged Navier–Stokes (RANS) formulation by Tse and Hall [15], who found that a sub-optimal match between the BLI propulsor and the fuselage can exacerbate flow separation and reverse flow, jeopardising the theoretical propulsive gain.

Mennicken et al. [16] conducted parametric studies on BLI fan design parameters combining throughflow methods and 3D CFD at multiple mission points, concluding that a higher than typical tip speed is necessary to increase the characteristic slope and limit the operating point excursion of the blades. Martensson [17] examined the effect of BLI distortion forced response on the fan blades aeromechanics, which is particularly challenging in terms of aeroelastic behaviour and mechanical resistance, as highlighted by Celestina and Long-Davis [18] for the NASA BLI2DT distortion tolerant fan [19]. Min et al. indicated blade mistuning as an important source of observed vibration levels in wind tunnel tests [20].

Sieradzki et al. [21] designed and experimentally tested a BLI fan, pointing out the challenges in the numerical modelling, with an optimistic performance predicted by CFD against experiments and a significant stall margin drop compared to clean inflow. Wernick et al. [22] applied different optimisation algorithms to a BLI fan, succeeding to improve the adiabatic efficiency at a small expense of total pressure ratio.

Aiming to explore design solutions that can help keeping high levels of efficiency while contributing to stabilise the fan operation across the continuously changing inflow conditions arising at cruise, in this paper we present a method for the design optimisation of fan blade profile in BLI applications. The study is an extended version of a conference paper presented at the 16th European Turbomachinery Conference (ETC16) [23] and illustrates a framework for the optimisation of quasi-2D profiles operating in the transonic regime. A

multi-point and multi-objective problem is solved to maximise the compression efficiency at a fixed inflow Mach number and total pressure ratio and the stall pressure ratio at a lower relative Mach number. The results for two transonic conditions are presented and analysed. With selected Pareto solutions, the profiles are stacked in a full-span three-dimensional blade operating with a realistic BLI inlet flow. The rotor is first simulated under different axisymmetric inflow conditions using a steady-state single-passage model and then with an unsteady full-annulus sliding mesh solution, comparing the flow field and the performance obtained in the different cases. The geometric models, the algorithms devised for blade section optimisation, and the computational methods are described in the next Section 2 of the paper. Section 3 presents and discusses the results. The overall outcome and outlooks of the study are summarised in the concluding Section 4.

2. Methods

The study considers two-dimensional profiles of compressors with transonic relative inlet Mach number, to be adopted in the upper span of low-pressure ratio fans used in BLI propulsion. The geometric representation of the blade sections and the numerical models employed for their simulation are described below.

2.1. Blade Parametric Module

The blade geometries employed for sectional and three-dimensional studies were built using a fully parametric model using the TMBM3.0 in-house software. The code can deal with generic axial, radial, or mixed type turbomachinery and builds the geometry by applying a specified blade sectional shape at constant-span layers, by subdividing the meridional blade projection, as illustrated in Figure 1. The hub, shroud, inlet, outlet, leading edge and trailing edge meridional projections (Figure 1a) are described as B-Splines, shaped through the position of their control points, shown with circles in the sample figure. Constant-span "streamlines" are depicted with dashed lines and each is parametrised as a curve

$$s(m) = [z(m), r(m)] \tag{1}$$

where

$$dm^2 = dz^2 + dr^2 \tag{2}$$

is the arc length coordinate of the streamline. For each constant span line, the blade section is represented by the camberline slope and the thickness distribution. The first is expressed in this study as

$$\beta = \beta(m') \tag{3}$$

with

$$dm' = \frac{dm}{r} \tag{4}$$

and

$$tan(\beta) = r\frac{\partial \theta}{\partial m} \tag{5}$$

The chord-normalised thickness distribution

$$t/c = \frac{t(m)}{c} \tag{6}$$

(shown in Figure 1b with the B-Spline control polygon) is applied normal to the camberline in the $m - r\theta$ plane (Figure 1c to give the constant-span profile). The blade sections from hub to shroud are then used to build a three-dimensional B-Spline surface giving the final blade.

https://doi.org/10.3390/ijtpp11020018

For the individual blade section optimisation, reported in Section 3.1, nine decision variables were adopted: six to control the camberline, and three to control the thickness. In both cases, the distribution was altered by manipulating the B-Splines control points. For the thickness, its maximum value and its chord-wise position were set with two design variables, and a third was used to control the thickness slope in the first quarter of chord, which is critical in supersonic profiles.

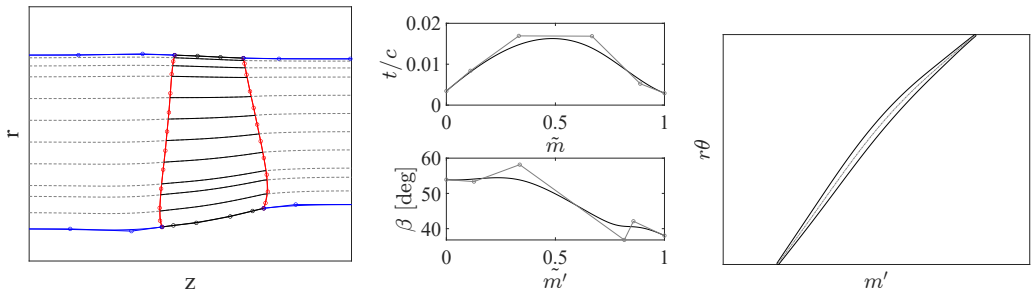

Figure 1. Blade parametric module. (**a**) Meridional plane. (**b**) Thickness and camberline distribution. (**c**) Blade section.

2.2. Numerical Model

The numerical model of the fan rotor was based on established industrial CFD practice employing Reynolds-Averaged Navier–Stokes (RANS) $\kappa - \omega$ SST [24] closure, previously validated against three-dimensional transonic rotor designs [25]. For blade section optimisation, quasi-2D simulations were solved within a stream sheet channel representing a single blade passage of varying height H, to model a non-unitary Axial Velocity Density Ratio (AVDR) $AVDR = (\rho_2 V_{ax,2})/(\rho_1 V_{ax,1}) = H_1/H_2$, with 1 denoting the inlet of the domain, and 2 the outlet. The rotor was enclosed in a body-fitted, structured multi-block grid connected to a structured quadrilateral inlet and outlet blocks, the rotor motion simulated by an implicit mixing plane model to avoid reflections in the stationary-rotational domains interface. The height of the first wall cell was set to have a non-dimensional distance $y^+ < 1$. The inlet and outlet boundaries were places 4.5 axial chords far from the rotor, following the outcome of the CFD validation of a transonic compressor linear cascade carried out in [26]. Grid stretching was adopted close to the boundaries to reduce numerical reflections. A sample mesh is shown in Figure 2.

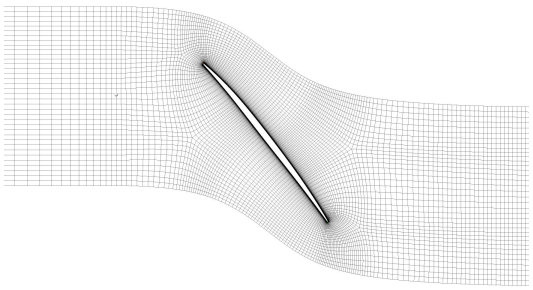

Figure 2. Sample mesh for blade profile.

Such an approach had been previously validated for purely 2D blade optimisation in linear cascades, where the relative flow field was simulated [26]. In the current quasi-2D model with rotational periodic boundaries at the blade passage sides, total pressure, total temperature, and velocity direction were set at the inlet of the computational domain. At the outlet, the static pressure was set, producing a mass flow rate that fulfilled the unique

incidence condition. For a given blade geometry, in fact, the inflow state $M_1, \beta_1, M_2 = f(p_1^0/p_2, \Omega)$, with β as the relative flow angle, is determined from the unique incidence after setting the boundary conditions: inlet total pressure p_1^0, outflow static pressure p_2, and blade rotational speed Ω. This approach of specifying the boundary conditions as pressure-inlet/pressure-outlet removes the need for a unique-incidence enforcement scheme [26] but still requires iterations to match specific conditions as highlighted later.

The sensitivity to the grid size for quasi-2D simulations was assessed by systematically varying the number of grid nodes N through a uniform refinement. The results are shown in Figure 3, from which it appears that the overall change of efficiency and mass flow rate is very limited, and the flow field stabilises for a characteristic size below 2×10^{-3}. The Grid Convergence Index (GCI) [27] between the two finest levels was 1.58×10^{-4} and 7.33×10^{-5} for the isentropic efficiency at OP_1 and OP_2, respectively. For the mass flow rate, the same indexes were 4.24×10^{-4} and 2.26×10^{-7}. Therefore, the small GCI indicated that the extrapolation error on grid convergence was sufficiently small enough to allow retaining the grid level with the characteristic size of 2×10^{-3} for the following analyses.

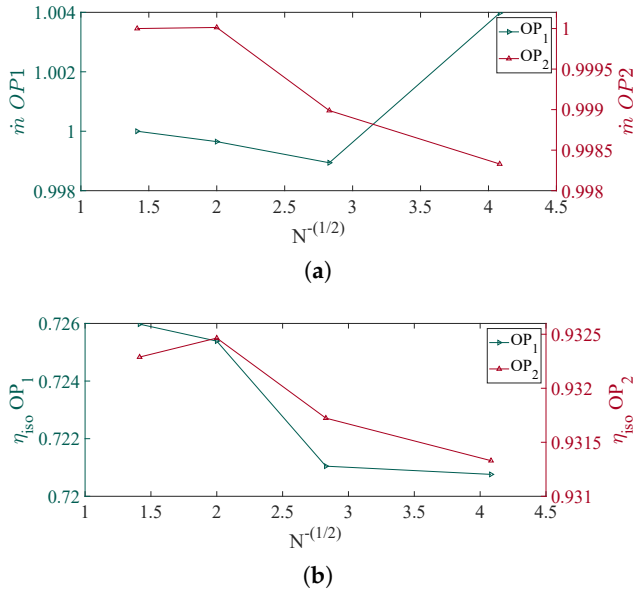

Figure 3. Blade profile grid sensitivity study. (**a**) Mass flow rate. (**b**) Isentropic efficiency.

For three-dimensional simulations, either single-passage steady-state solutions or full-annulus unsteady solutions were used. The same meshing strategy of the sectional blade analysis was retained, with the structured body-fitted multi-block mesh around a single passage having 1.2 M cells. The choice derived from a grid sensitivity study on a baseline geometry, where the mesh size was systematically varied by uniformly reducing the characteristic cell size. The assessment showed the convergence of integral metrics from the medium to the fine mesh as reported in Figure 4. The boundary conditions were a pressure inlet, in which the spatial distribution of the stagnation pressure and temperature were specified, and a pressure outlet, where the static pressure distribution varied according to a radial equilibrium law. For unsteady RANS solutions, the initial condition was set by replicating a single-passage solution obtained with an axisymmetric inflow condition. Temporal periodicity of the flow field occurred after five rotor revolutions, and statistics of integral metrics were accumulated over two complete rotor revolutions for averaging. For the time discretisation, a backward second-order method was used with a relatively coarse time-step, allowing to resolve without aliasing seven blade passing frequencies. The purpose of the unsteady analysis was, in fact, to obtain a preliminary estimate of the

integral machine performance and the flow field topology across the cascade, rather than a highly resolved analysis of the temporal length scales occurring.

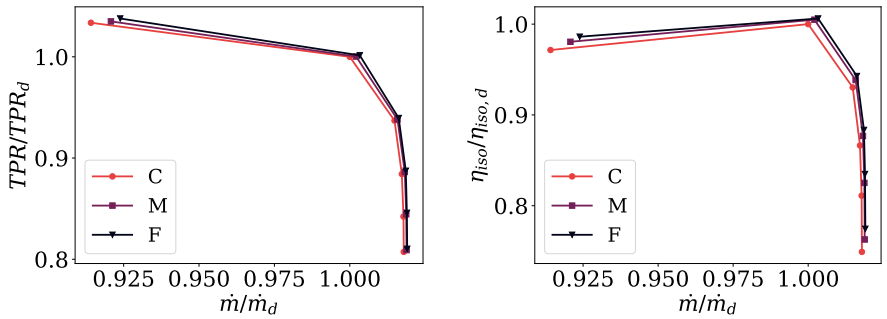

Figure 4. Sensitivity of characteristic maps to grid size for a sample three-dimensional blade. (**a**) TPR. (**b**) η_{iso}.

2.3. Optimisation Strategy

The operation of a fan in a non-uniform total pressure environment induces several effects on the flow field. Authors in the literature, using numerical and experimental methods, have identified key physical mechanisms driving the blade response to inlet distortion [28–30]. In view of these findings, considering the specific case of a rear-fuselage boundary layer ingesting propulsor, the resulting inlet field is characterised by a continuously changing total pressure profile and flow swirl, caused by the up-swept fuselage boundary layer (an example from a CFD simulation of an aft-fuselage BLI nacelle will be showed later). The rotor thus has to operate under low-momentum areas corresponding to reduced mass flux, i.e., inlet Mach number, and high-momentum areas, i.e., higher inlet Mach number, passing over one rotation multiple times from post-stall to deep choking conditions.

In order to enhance the capability of the rotor to efficiently and safely operate in such a scenario, an optimisation problem for blade profile sections in the upper half of the blade span was solved considering two operating points (OP), denoted OP_1 and OP_2. OP_1 is the design operating conditions, where a target total pressure rise value is required at a prescribed relative inlet Mach number (the Mach number will be implicitly assumed to be in the rotor relative frame from here on). OP_2 is a near-stall operating point, occurring at a lower than design Mach number, representing the profile operation in a low momentum region, where at the same time a lower relative M_1 and a higher blade incidence occurs, the passage being operated unchoked.

Due to the setup of the computational domain, solving both the absolute and the relative flow motion, it was necessary to devise an algorithm to replicate the desired operating conditions for quasi-2D blade sections. In fact, neither the incidence angle, or equivalently β_1, nor the Mach number M_1 could be directly specified, both coming from the unique incidence condition. The proposed algorithm works differently for the two OP. For OP_1, the workflow is reported in Figure 5. For a given p_1^0, the following relationships hold:

$$M_1, \beta_1, M_2 = f(\Omega, p_2/p_1^0) \tag{7}$$

$$\begin{aligned} TPR &= p_2^0/p_1^0 \\ &= p_2^0(M_2, p_2/p_1^0)/p_1^0 \\ &= p_2^0(\Omega, p_2/p_1^0)/p_1^0 \end{aligned} \tag{8}$$

Given that $\frac{\partial \beta_1}{\partial p_2} = 0$ and $\frac{\partial M_1}{\partial p_2} = 0$ at the design point since the blade passage is choked and unique incidence holds because $M_1 > 1$, the target couple $(M_1^{tgt}, p_2^0/p_1^0 = TPR^{tgt})$ can be found as a function of the corrected rotational speed Ω and back-pressure p_2 (Ω, p_2) with:

$$M_1^{tgt} = M_1^j + \left.\frac{\partial M_1}{\partial \Omega}\right|_j (\Omega^{j+1} - \Omega^j) \tag{9}$$

$$TPR^{tgt} = TPR^j + \left.\left(\frac{\partial TPR}{\partial \Omega}, \frac{\partial TPR}{\partial p_2}\right)\right|_j \cdot \left(\Omega^{j+1} - \Omega^j, p_2^{j+1} - p_2^j\right) \tag{10}$$

As shown in the diagram, the derivatives $\frac{\partial M_1}{\partial \Omega}$, $\frac{\partial TPR}{\partial p_2}$, and $\frac{\partial TPR}{\partial \Omega}$ can be computed by finite difference between two consecutive simulations j and $j-1$, allowing to extrapolate the required value of Ω^{j+1} and p_2^{j+1} giving the target M_1^{tgt} and TPR^{tgt}. In each iteration j, therefore, the blade row is solved with a the specified couple Ω^j and p_2^j, finding M_1^j and TPR^j. If they are not within a threshold with their target values, by using the stored data of the current and previous iteration the derivatives of the input parameters with respect to these output quantities are calculated by finite difference, and a new couple Ω^{j+1} and p_2^{j+1} is extrapolated. With a first estimate of the derivatives coming from a Design of Experiment (DOE) campaign used to initialise the optimisation, the algorithm was able to meet the targets at OP_1 with a 2% absolute error within four iterations. An optimal tuning of the CFD solution, along with a suitable choice of residual target and number of iterations (the derivatives do not require a fully converged CFD solutions but only a stabilisation of the integral metrics upon which they depend), allowed to obtain affordable computational times.

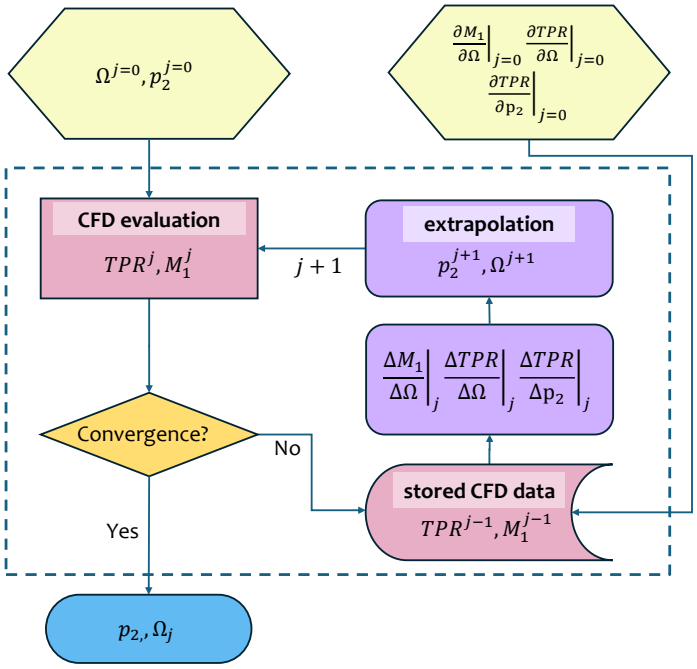

Figure 5. Workflow to enforce boundary conditions at $OP1$ with choked blade passage subjected to the unique incidence condition.

At OP_2, the near-stall condition has an unchoked blade passage, with M_1 and β_1 varying independently from p_2 at given Ω and p_1^0. Here, the rotational speed Ω^{OP_2} was set fixed to give a unique incidence Mach number $M_1^{OP2} \approx 0.9 M_1^{OP1}$ using the last evaluated sensitivity $\frac{\partial M_1}{\partial \Omega}$ at OP_1 and the near-stall condition was found with a grid search algorithm

with an adaptive p_2 step, letting a maximum number of iterations equal to four. Using the same optimised numerical strategy, the computational time for OP_2 was comparable to that for OP_1.

The formal optimisation problem was thus formulated as

$$\min \mathbf{F}(\mathbf{X}) = \begin{cases} f_1(\mathbf{X}) = -\eta & @OP_1 \\ f_2(\mathbf{X}) = -TPR_{max} & @OP_2 \end{cases} \quad (11)$$

with $\mathbf{X}$ denoting the design variable vector, containing six B-Spline control points vertical displacements of the camberline β distribution and three B-Spline control points displacements of the thickness distribution. The latter was varied in terms of compression ramp slope, leading edge radius, and maximum thickness value. Thus, a total of nine design variables was used for each profile. The proprietary GeDEA-II genetic algorithm was used to solve the multi-point multi-objective optimisation problem, due to its superior performance for constrained multi-modal functions [31].

In order to ensure that at the p_1^0/p_2 of OP_1 the blade did not stall prematurely at OP_2, a constraint on the stall back-pressure p_2 of OP_2 was added, requiring $p_2^{OP_2} > p_2^{OP_1}$, meaning that at given p_1^0, the design outflow static pressure p_2 of OP_1 must not cause stall at a lower inlet Mach number (OP_2).

3. Results

3.1. Blade Profile Optimisation

The nine decision variable problem of finding the Pareto-optimal solutions of camberline and thickness distribution according to the specified multi-objective and multi-point formulation was solved with the target conditions reported in Table 1, corresponding to those met near the tip of a typical transonic fan. Each case had an AVDR = 1.15 and was run for 10 generations with a population size of 20 individuals.

Table 1. Operating conditions for profile optimisation.

M_1 @ OP_1	TPR @ OP_1
1.10	1.38
1.05	1.35

The summary result in terms of the Pareto frontier is reported in Figure 6 for the two cases. The case with $M_1 = 1.10$ has a narrower Pareto front, with a lower variation of the objectives. In both cases, the conflict between them is evident. Selected Pareto points, going from the best in f_1 to the best in f_2, are examined in the following.

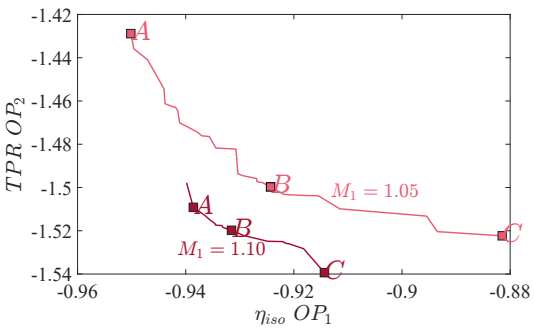

Figure 6. Pareto front of the blade profile optimisations.

Figure 7 reports the camberline slope β and thickness distribution t/c for the three points, marked A, B, and C in Figure 6. Opt. A corresponds to the best efficiency airfoil, at

expense of stall TPR, and it is very similar to the best compromise solution B. Both have an S-shaped pre-compression ramp and a low thickness. The best stall-TPR profile, Opt. C, has a very low thickness in the fore part and a higher deflection on the trailing edge.

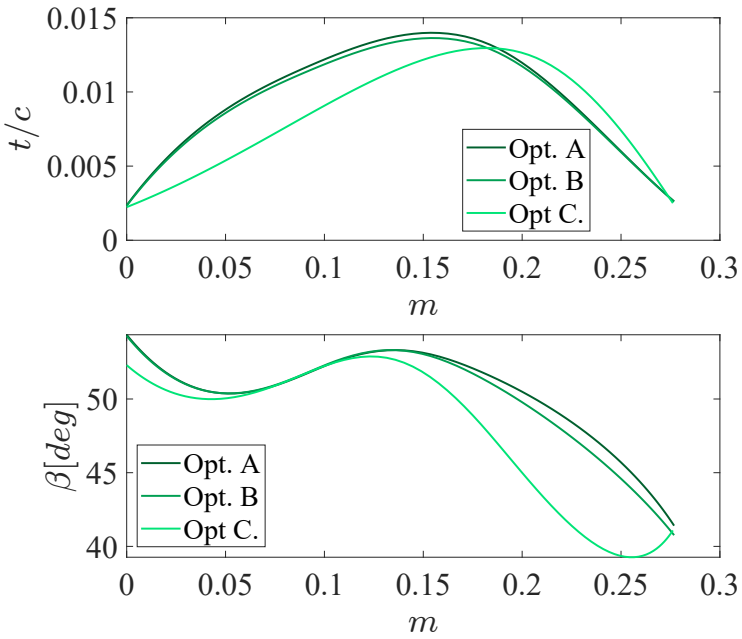

Figure 7. Camberline slope and thickness distribution for selected Pareto points for $M_1 = 1.1$.

The performance of Opt. A and Opt. C can be appreciated by looking at the Mach number contours of Figure 8. At OP_1, Opt. A has a weak bow shock impinging on the suction surface near the trailing edge, where an inclined mild passage shock originates. Opt. C has a similar shock pattern, although the higher deflection creates a stronger passage shock and a thicker wake eroding the efficiency. At OP_2, the slope of Opt. A causes a strong detached shock, triggering boundary layer separation on the suction surface. Opt. C has a less detached and weaker bow shock due to a reduced expansion from the leading edge, and the attached flow is more turned, producing a higher pressure ratio at stall.

At $M_1 = 1.05$, Figure 9 shows the camberline slope and thickness distributions of the three selected points on the Pareto. The shapes are now more various, with Opt. A being an S-shaped profile, Opt. B having a balance in both objectives featuring a less pronounced counter-slope at the fore chord, and Opt. C having a single curvature. This trend appears more regular and indicative of a physical mechanism. The thickness distributions are very similar, instead, with Opt. C presenting a slightly increased thickness in the first 20% of chord.

The Mach number distribution of Opt. A against Opt. C is depicted in Figure 10. In the former, the shock/expansion pattern resembles the one in Figure 8a at OP_1, with a weak bow shock and an even weaker passage shock causing no harm to the boundary layer. Opt. C has a merged bow and passage shock, with a large suction side separation which increases the losses. At OP_2, Opt. C shows improved performance with a mild tail separation triggered by the ejected passage shock, the flow deviation at the trailing edge raising the total pressure. Opt. A, instead, suffers from a strong detached shock far from the leading edge which is induced by the higher acceleration, showing less tolerability to increased back-pressure.

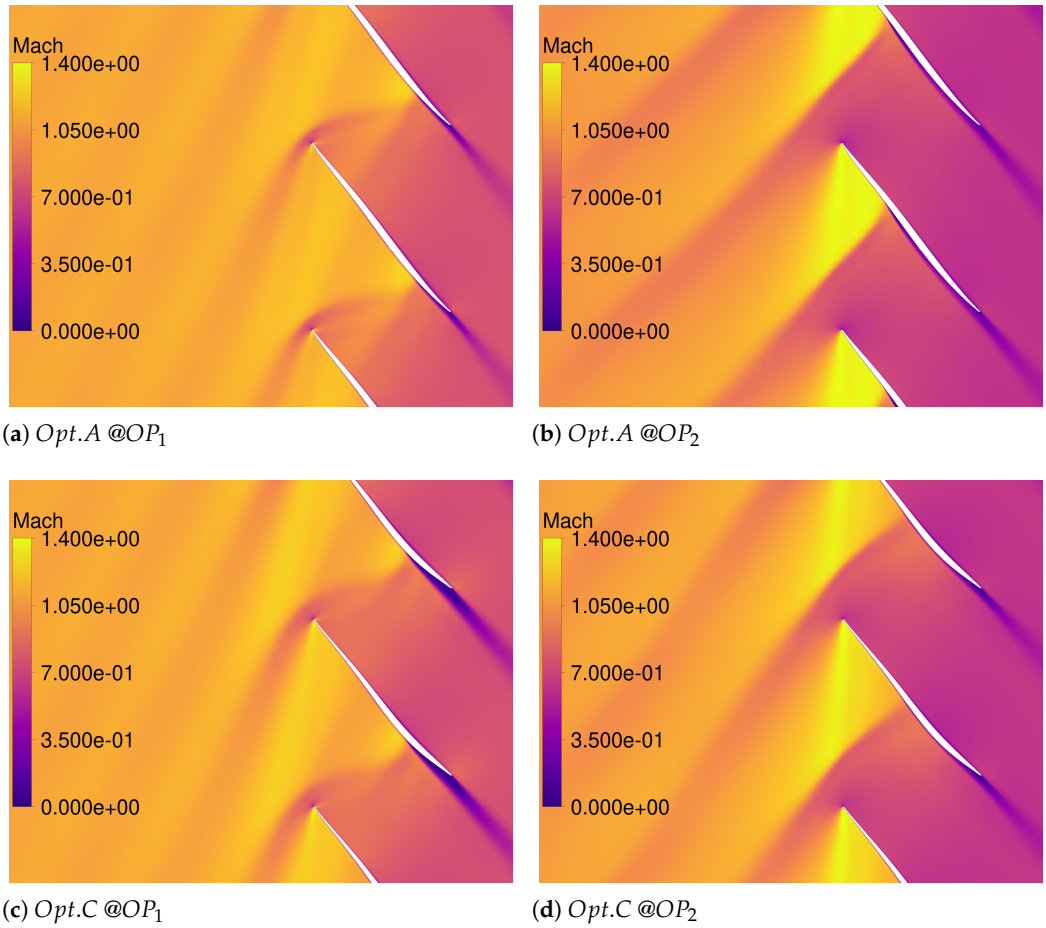

(**a**) $Opt.A$ @OP_1 (**b**) $Opt.A$ @OP_2

(**c**) $Opt.C$ @OP_1 (**d**) $Opt.C$ @OP_2

Figure 8. Selected optimised profiles for $M_1 = 1.1$. Relative Mach number distribution. (**a**) $Opt.A$ @OP_1. (**b**) $Opt.A$ @OP_2. (**c**) $Opt.C$ @OP_1. (**d**) $Opt.C$ @OP_2.

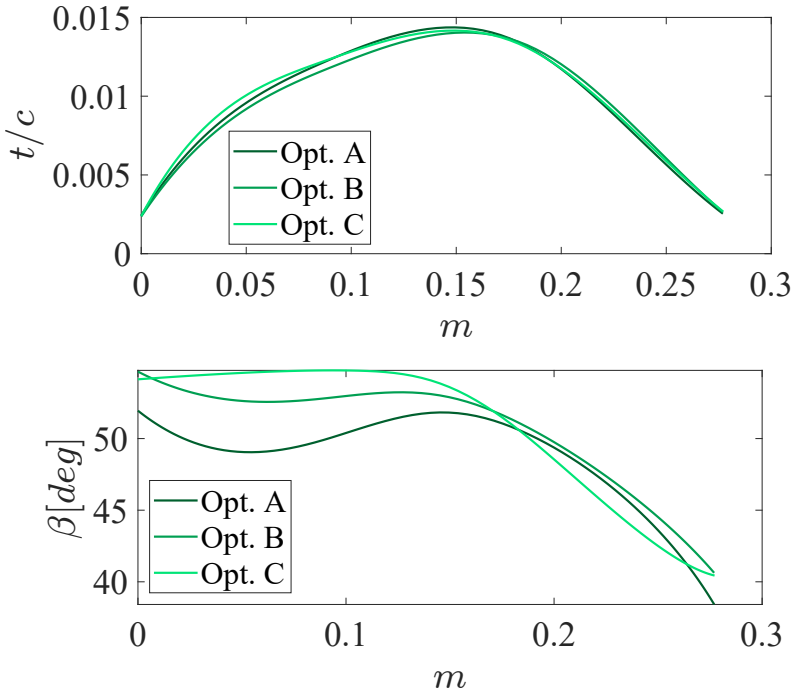

Figure 9. Camberline slope and thickness distribution for selected Pareto points for $M_1 = 1.05$.

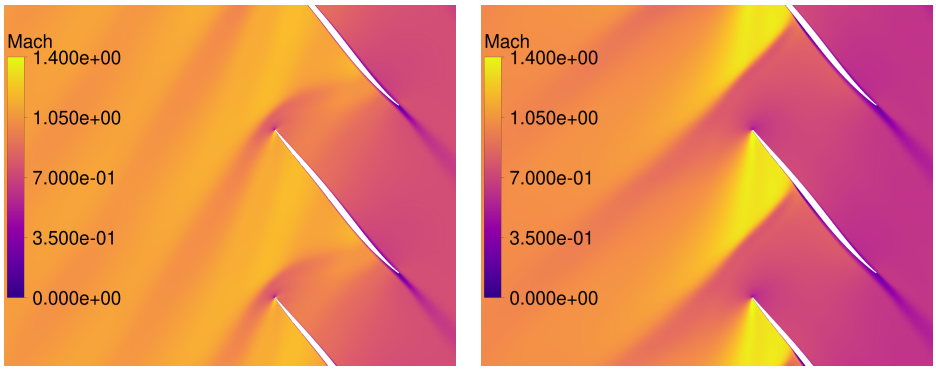

(**a**) *Opt.A @OP*$_1$ (**b**) *Opt.A @OP*$_2$

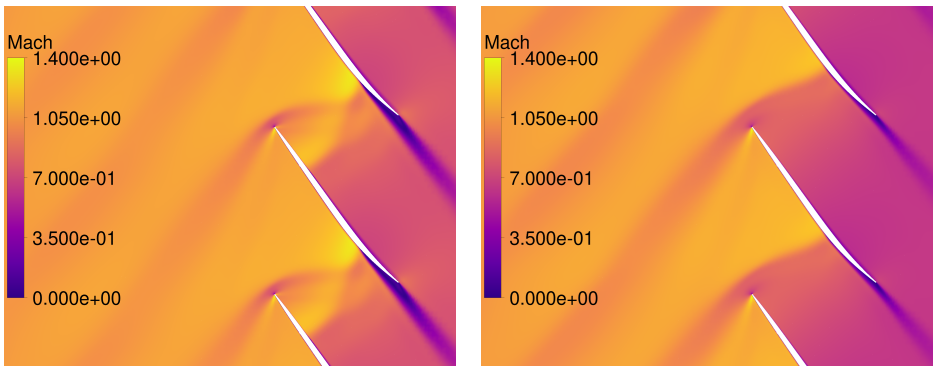

(**c**) *Opt.C @OP*$_1$ (**d**) *Opt.C @OP*$_2$

Figure 10. Selected optimised profiles for $M_1 = 1.05$. Relative Mach number distribution.

Overall, the outcome of the sectional optimisations indicates a certain trend of Pareto solutions, with an expected S-shaped fore part for higher efficiency and large deflections for maximum TPR, which substantially agrees with previous research on transonic compressors [32].

3.2. Three-Dimensional Assessment

The result of the previous quasi-2D blade optimisation was utilised for a preliminary three-dimensional assessment using a full-span blade model, in order to analyse the flow field arising when including the effect of radial flows and under inlet distortion typical of a BLI application. The latter was obtained from the CFD simulation of a half-wing aircraft model with aft-fuselage BLI propulsor in cruise condition [33]. The total pressure field is depicted in Figure 11, together with three insets showing the radial distribution at three azimuthal positions. The fan blade was designed for a pressure ratio of 1.31 and a tip Mach number of 1.10, with profiles from sectional optimisations employed above 87.5% of span.

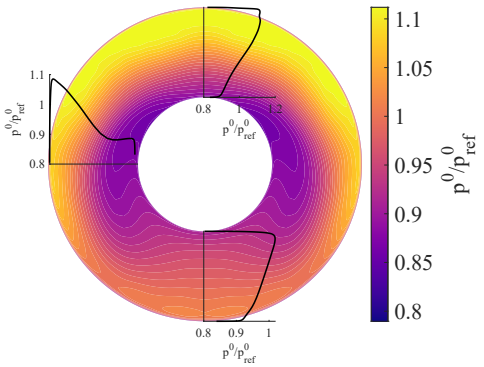

Figure 11. Inflow condition used in three-dimensional blade evaluation.

For the assessment of the three-dimensional performance, different approaches were used. Initially, single-passage steady-state simulations were run with axisymmetric distributions of total pressure at the inlet. The rationale stemmed from the fact that when the purpose is to evaluate the integral metrics of the turbomachinery in a rapid way, an approach similar to a frozen-rotor model might be used. Since the inflow conditions are continuously changing as a single blade rotates, the aerodynamic interface plane (AIP) can be sampled at a given azimuthal coordinate, equivalent to the phase angle of the blade, in order to reconstruct the overall performance through the combination of several single-passage steady-state simulations with different blade clocking. Such an approach is similar to the parallel compressor (PC) method, which in its simplest formulation computes the operating point as the area-weighted average on the distortion sector amplitude of the working condition obtained on the clean characteristics with different inflow total pressure and equal outlet static pressure [34]. A further simplification consists in computing the integral machine performance by considering an equivalent axisymmetric inflow condition, rather than combining results obtained with different boundary conditions. This approach neglects the flow redistribution induced by the non-uniform static pressure on the AIP and assumes that co- and counter-swirl regions globally compensate. The possibility of deriving the integral performance of the turbomachinery in this way was tested using the circumferentially averaged spanwise distribution of total pressure extracted from the AIP. The flow field is shown in Figure 11, along with spanwise profiles extracted on the crown, keel, and sideline. The solution was thus obtained either with the circumferential-average spanwise profile and with the profiles extracted at these three locations.

Figure 12 reports the characteristic maps obtained by varying the outlet static pressure with single-passage simulations under the different inlet conditions. The azimuthal angle θ starts from the top dead centre in Figure 11 and runs counter-clockwise in the figure. It can be observed that the curve obtained by combining the radial profiles with the parallel compressor average strictly follows the one obtained with the circumferential-averaged radial profile, both in terms of TPR and η_{iso}, although with a small offset which is quantified in about 0.5% for the total pressure ratio and lower than 1% for the efficiency. This indicates that the two methods are consistent for the specific inflow condition considered, despite both being rather simplified. In particular, the true parallel compressor method requires to consider several physical effects taking place, like the impact of the critical distortion sector and inertial phenomena [34,35]. On the other hand, the approach tested here is not strictly a parallel compressor method, of which it only uses the area-weighted average based on the distortion amplitude to combine the solutions of different radial profiles. A more realistic assessment requires comparison with higher fidelity simulations accounting for the effect of the distortion. For this reason, in addition to single-passage solutions, the time-averaged integral metrics are also shown for the URANS simulation. In terms of TPR, the URANS provides a value of 1.27, which is about 1.5% lower than the circumferential-averaged inflow with the same mass flow rate. For the efficiency, the value is 0.5% lower, in the same condition. The result thus confirms that it can be possible to obtain a preliminary estimate of the integral machine performance using a simplified method which relies only on an axisymmetric inlet profile.

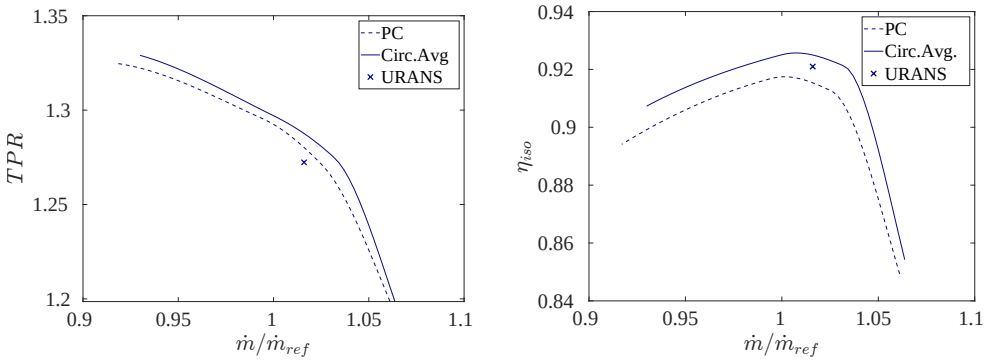

(**a**) (**b**)

Figure 12. Characteristic maps for 3D fan geometry obtained with different models. (**a**) TPR. (**b**) η_{iso}.

By also examining the local parameters, the differences between the models can be further appreciated. Figure 13a reports the spanwise distribution of TPR under different inflows at near peak efficiency, including the URANS solution. Starting from the curves for constant azimuthal sampling of the AIP total pressure, due to the largely varying distribution on the inlet, shown in Figure 11, the turbomachinery reacts with different work input and compression. In the case of $\theta = 90°$, the large total pressure deficit below mid span forces the blades to operate at lower mass flow rate closer to the stall, with higher work input, as seen by the work coefficient $\psi = \Delta H^0 / \left(\Omega r_{tip}\right)^2$ in Figure 13b. The same conditions hold in the case where $\theta = 180°$ above mid span, where the higher total to static pressure ratio results in increased compression, whereas the opposite occurs below mid span, where the energy exchange is reduced. The circumferential-averaged inflow and the URANS curves are instead in good agreement, again confirming the result previously obtained for integral metrics, also in terms of local distribution.

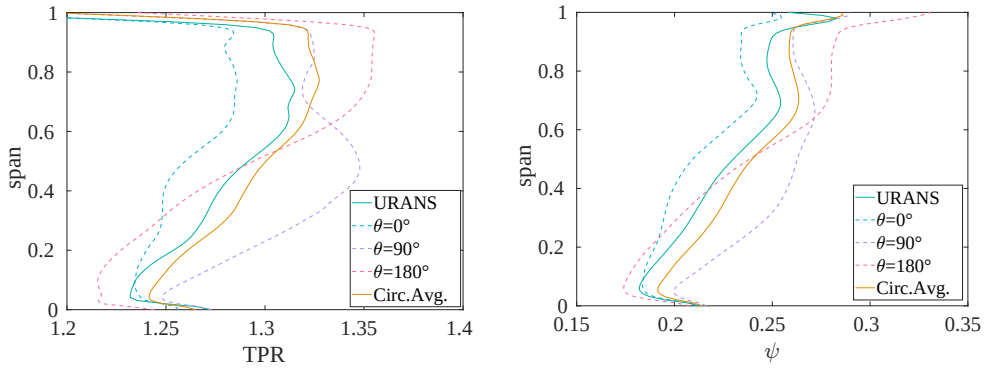

(**a**) (**b**)

Figure 13. Spanwise distribution of circumferential-averaged quantities at rotor outlet with different models. (**a**) TPR. (**b**) ψ.

As observed in the sectional optimisation, when operating under the full-annulus inflow, blade profiles are subject to a variety of conditions covering a wide operating range. Figure 14 shows the instantaneous relative Mach number distribution at 92.5% obtained in the URANS simulation. The flow field results from the superposition of several effects, related to the non-uniformity of total and static pressure, which induces flow redistribution upstream of the blades. This, in turn, generates a non-homogeneous mass flux and blade incidence due to pre-swirl. In the figure, the variation of the relative inlet Mach number along the circumference can be appreciated, together with the change of the shock-wave pattern across the cascade, which rotates from left to right in the figure. On the left-hand

side, a strong normal passage shock impinging on the trailing edge is present. Its position shifts upstream as the inlet Mach number reduces and the total-to-static pressure ratio from inlet to outlet increases, until it merges with the bow shock. This condition corresponds to the maximum work input of the blades. Continuing towards right, the higher inlet Mach number pushes the cascade to operate with larger mass flux and lower energy exchange. The passage shock re-enters into the channel, until it greatly weakens, leaving only the bow shock as the primary shock structure. Proceeding towards the right-hand-side, the situation returns back to the high work input, and the passage shock strengthens. The blade profiles are thus subject to a significant operating point excursion even at near-design conditions, which justifies the previous sectional optimisation aimed at extending their operational regime.

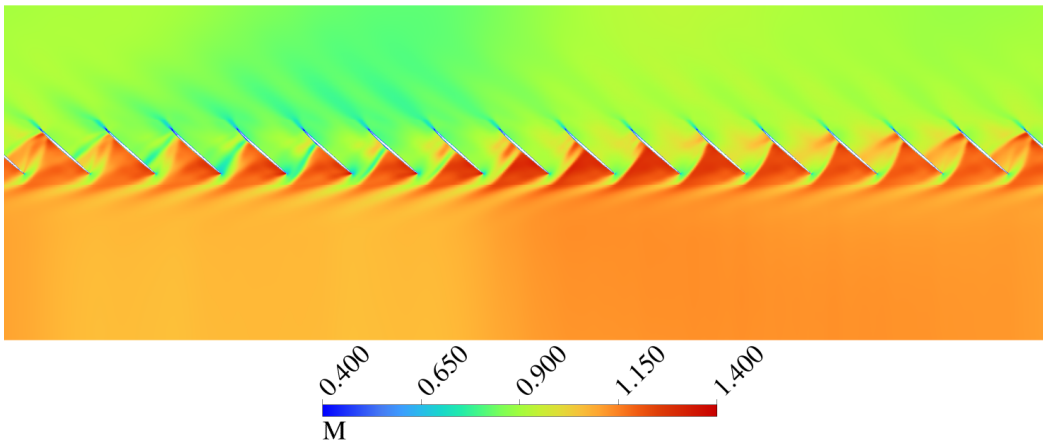

Figure 14. Instantaneous relative Mach number distribution at 92.5% of blade span.

Downstream of the rotor, the flow field assumes specific features deriving from the blade response to inlet distortion. In particular, the cascade reacts with a non-uniform work input, as previously highlighted, which tends to make the circumferential distribution of total pressure more even. This can be appreciated in Figure 15a, showing the ratio between the outlet total pressure to the mass flow averaged inlet value. Near the hub, the fuselage upsweep creates symmetric low total pressure regions, see Figure 11. The outflow distribution is azimuthally smoother, although the co-swirl and counter-swirl respectively augments and diminishes the total pressure in the left and right sides of the hub. The flow in the upper span also has two higher compression lobes, although not in phase with those below mid span. Flow losses are visualised by means of the entropy loss function $\xi = 1 - e^{-(s_2 - min(s_1))/R}$. Two main mechanisms appear in Figure 15b. The first one is related to wake losses. Wakes inside the low inlet total pressure lobes are thicker and more dissipating, extending in a relevant fraction of the span. The second mechanisms is related to the tip leakage flow, whose vortex increases from the bottom left corner (blade rotation is in the counter-clockwise direction in the figures) due to the large operating point shift near the tip. This second effect is obviously not accounted for in the sectional optimisation, and it has been analysed more in depth by other authors in the literature [36].

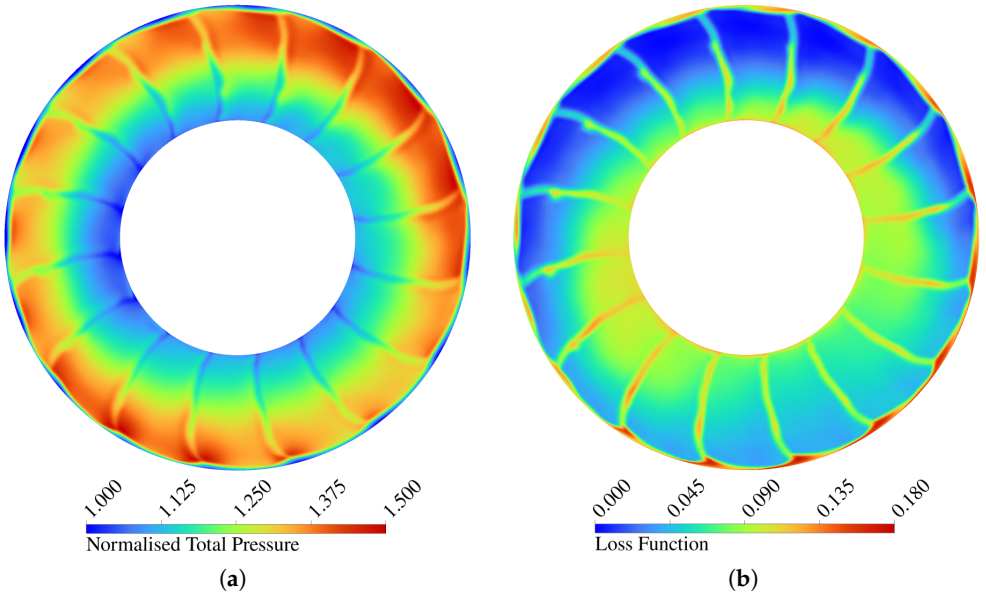

Figure 15. Instantaneous flow field at rotor outlet. (**a**) $p_2^0/\overline{p_1^0}$, (**b**) $\bar{\zeta}$.

4. Conclusions

An optimisation strategy for quasi-2D transonic fan blade section optimisation targeting multiple operating conditions in a multi-objective fashion has been presented. The methodology relies on maximising the efficiency at a fixed inflow relative Mach number by an adaptive algorithm, and maximising the stall TPR at a lower relative Mach number, mimicking what happens during the blade rotation in a distorted field of a tail BLI propulsor installation. The sectional optimisation under different inlet conditions, comprising an unchoked passage, partially includes the operation of the profiles with varying incidence and thus pre-swirl. The algorithm has proven effective in identifying the design conditions where the inlet Mach number and the TPR must be achieved, reaching good computational efficiency.

The analysis of Pareto solutions has shown a trend for mild pre-compression ramp in the leading edge for higher efficiency, with straighter profiles having a more deflected trailing edge for higher stall pressure ratio. For this second objective, the maximum back-pressure tolerable by the blade varies for each individual. A future improvement will be the replacement of the grid search algorithm with a more accurate method, like a bisection, since the resolution on the stall TPR is limited by the minimum step of the search algorithm, but a small percentage variation in p_2/p_1^0 can result in further change of TPR at stall.

With selected optimal airfoils, a preliminary three-dimensional analysis on a transonic fan operating in a realistic BLI inflow has been conducted. The large excursion of the operating point of blades during their rotation observed in the URANS simulation corroborates and justifies the sectional optimisation approach, which considers two relative inlet Mach numbers and working regimes. Even in the design condition, the blades are subject to a continuously varying inflow that requires high tolerance to incidence, Mach number and total-to-static pressure ratio variation, which can be addressed for starting from the blade section design.

For the inlet distribution considered, simplified modelling approaches based on single passage simulations have also been tested, to explore the possibility of obtaining integral performance metrics at a reduced computational time. For the specific inflow condition considered, the circumferentially averaged spanwise distribution of total pressure has been found to provide a result fairly close to the URANS simulation, in terms of global and radial variables. This indicates that that axisymmetric inflow profile is representative of the average

operating condition of the blade passages under distortion. Further investigation is required to determine whether this outcome can be generalised and its dependency upon the intensity of the azimuthal gradients on the inflow plane. Nonetheless, it can provide a useful indication for preliminary estimation of the machine performance in a design exploration study. Similarly, the combination of results obtained with different spanwise profiles can be further examined, by merging data with the complete parallel compressor method, which can account for the combination of total pressure and swirl distortion on the AIP.

Finally, the design of a distortion tolerant fan blade confirms to be a challenging task when targeting high isentropic efficiency with the necessary stability. The adoption of advanced numerical methods can help with scanning the design space for optimal combinations of two-dimensional and three-dimensional blade properties. However, the large number of variables and the need to tailor the aerodynamic design on specific working conditions still leaves many open questions that need to be addressed by the scientific and industrial communities.

Author Contributions: Conceptualisation, A.M.; methodology, A.M.; software, A.M.; validation, A.M.; formal analysis, A.M.; investigation, A.M.; resources, A.M. and E.B.; data curation, A.M.; writing—original draft preparation, A.M.; writing—review and editing, A.M.; visualisation, A.M.; supervision, E.B. All authors have read and agreed to the published version of the manuscript.

Funding: This research received no external funding.

Data Availability Statement: The data presented in this study are available upon reasonable request from the corresponding author.

Acknowledgments: The author acknowledges the CINECA award under the ISCRA initiative, for the availability of high performance computing resources and support.

Conflicts of Interest: The authors declare no conflicts of interest.

Abbreviations

The following abbreviations are used in this manuscript:

c	chord
H^0	total enthalpy
M	relative Mach number
m	meridional coordinate
$\dot{m}$	mass flow rate
p	pressure
r	radius
s	entropy
t	thickness
$\mathbf{X}$	design variable
z	axial coordinate
β	camberline slope
η	efficiency
θ	azimuthal coordinate
ξ	entropy loss function
ψ	work coefficient
Ω	rotational speed
BLI	Boundary Layer Ingestion
CFD	Computational Fluid Dynamics
OP	Operating Point
PC	Parallel Compressor
TPR	Total Pressure Ratio

References

1. Diamantidou, D.E.; Hosain, M.L.; Kyprianidis, K.G. Recent Advances in Boundary Layer Ingestion Technology of Evolving Powertrain Systems. *Sustainability* **2022**, *14*, 1731. [CrossRef]
2. Hall, D.K.; Huang, A.C.; Uranga, A.; Greitzer, E.M.; Drela, M.; Sato, S. Boundary Layer Ingestion Propulsion Benefit for Transport Aircraft. *J. Propuls. Power* **2017**, *33*, 1118–1129. [CrossRef]
3. Uranga, A.; Drela, M.; Greitzer, E.M.; Hall, D.K.; Titchener, N.A.; Lieu, M.K.; Siu, N.M.; Casses, C.; Huang, A.C.; Gatlin, G.M.; et al. Boundary Layer Ingestion Benefit of the D8 Transport Aircraft. *AIAA J.* **2017**, *55*, 3693–3708. [CrossRef]
4. Moirou, N.G.; Sanders, D.S.; Laskaridis, P. Advancements and prospects of boundary layer ingestion propulsion concepts. *Prog. Aerosp. Sci.* **2023**, *138*, 100897. [CrossRef]
5. Seitz, A.; Habermann, A.L.; Peter, F.; Troeltsch, F.; Castillo Pardo, A.; Della Corte, B.; van Sluis, M.; Goraj, Z.; Kowalski, M.; Zhao, X.; et al. Proof of Concept Study for Fuselage Boundary Layer Ingesting Propulsion. *Aerospace* **2021**, *8*, 16. [CrossRef]
6. Bravo-Mosquera, P.D.; Cerón-Muñoz, H.D.; Catalano, F.M. Potential Propulsive and Aerodynamic Benefits of a New Aircraft Concept: A Low-Speed Experimental Study. *Aerospace* **2023**, *10*, 651. [CrossRef]
7. Uranga, A.; Drela, M.; Hall, D.K.; Greitzer, E.M. Analysis of the Aerodynamic Benefit from Boundary Layer Ingestion for Transport Aircraft. *AIAA J.* **2018**, *56*, 4271–4281. [CrossRef]
8. Lee, B.J.; Liou, M.F.; Celestina, M.; To, W. Benefit and Critical Factors for the Performance of the Boundary Layer Ingesting Propulsion. In Proceedings of the Turbo Expo: Power for Land, Sea, and Air, Online, 21 September 2020; Volume 2A: Turbomachinery, p. V02AT32A0. [CrossRef]
9. Gunn, E.J.; Hall, C.A. Aerodynamics of Boundary Layer Ingesting Fans. In Proceedings of the Turbo Expo: Power for Land, Sea, and Air, Barcelona, Spain, 8–11 May 2014; Volume 1A: Aircraft Engine; Fans and Blowers, p. V01AT01A024. [CrossRef]
10. Perovic, D.; Hall, C.A.; Gunn, E.J. Stall Inception in a Boundary Layer Ingesting Fan. *J. Turbomach.* **2019**, *141*, 091007. [CrossRef]
11. Lee, B.J.; Liou, M.F. Aerodynamic Design and Optimization of Fan Stage for Boundary Layer Ingestion Propulsion System. In Proceedings of the International Conference on Computational Fluid Dynamics (ICCFD 10), Barcelona, Spain, 9–13 July 2018. Available online: https://ntrs.nasa.gov/citations/20180005439 (accessed on 25 February 2026).
12. Battiston, A.; Magrini, A.; Ponza, R.; Benini, E. Fullscale Optimization and Fan Design of a Rear BLI Shrouded Propulsor. In Proceedings of the AIAA SCITECH 2023 Forum, Online, 23–27 January 2023. [CrossRef]
13. Pardo, A.C.; Hall, C.A. Design of a Transonic Boundary Layer Ingesting Fuselage Fan. In Proceedings of the Global Power and Propulsion Society, GPPS, Online, 24–28 August 2020; number GPPS-TC-2020. [CrossRef]
14. Castillo Pardo, A.; Hall, C.A. Effects of Sideslip Direction on a Rear Fuselage Boundary Layer Ingesting Fan. *J. Turbomach.* **2022**, *144*, 121012. [CrossRef]
15. Tse, T.S.; Hall, C.A. Aerodynamics and Power Balance of a Distributed Aft-Fuselage Boundary Layer Ingesting Aircraft. *Aerospace* **2023**, *10*, 122. [CrossRef]
16. Mennicken, M.; Schoenweitz, D.; Schnoes, M.; Schnell, R. Fan design assessment for BLI propulsion systems. *CEAS Aeronaut. J.* **2022**, *13*, 3–19. [CrossRef]
17. Mårtensson, H. Harmonic Forcing from Distortion in a Boundary Layer Ingesting Fan. *Aerospace* **2021**, *8*, 58. [CrossRef]
18. Celestina, M.L.; Long-Davis, M.J. Large-scale Boundary Layer Ingesting Propulsor Research. In Proceedings of the ISABE, Canberra, Australia, 22–27 September 2019; ISABE2019-24264.
19. Heinlein, G.; Dumlupinar, E.; Housman, J.A.; Jensen, J. Performance Characteristics of a Boundary Layer Ingesting Inlet—Distortion Tolerant Fan Through CFD Code Coupling. In *Proceedings of the AIAA SCITECH 2024 Forum, Orlando, FL, USA, 8–12 January 2024*; AIAA: Reston, VA, USA, 2024. [CrossRef]
20. Min, J.B.; Bakhle, M.A.; Duffy, K.P. Analysis of Blade Mistuning for Boundary Layer Inlet Flow Distortion-Tolerant Fan Blades. In Proceedings of the AIAA SCITECH 2024 Forum, Orlando, FL, USA, 8–12 January 2024. [CrossRef]
21. Sieradzki, A.; Kwiatkowski, T.; Turner, M.G.; Łukasik, B. Numerical Modeling and Design Challenges of Boundary Layer Ingesting Fans. *J. Turbomach.* **2022**, *144*, 111012. [CrossRef]
22. Wernick, A.R.; Chen, J.P.; Giuliani, J. Design Optimization of a Fan Blade under Boundary Layer Ingestion Flow. In Proceedings of the AIAA SCITECH 2023 Forum, Online, 23–27 January 2023. [CrossRef]
23. Magrini, A.; Benini, E. Optimising blade profiles to extend the operating range in BLI fan application. In Proceedings of the 16th European Turbomachinery Conference, Hannover, Germany, 24–28 March 2025; pp. 1–10.
24. Menter, F. Improved two-equation k-omega turbulence models for aerodynamic flows. In *Technical Memorandum 19930013620*; NASA: Washington, DC, USA, 1992.
25. Magrini, A. Body Force Model Implementation of Transonic Rotor for Fan/Airframe Simulations. *Aerospace* **2022**, *9*, 725. [CrossRef]
26. Casoni, M.; Magrini, A.; Benini, E. Supersonic Compressor Cascade Shape Optimization under Multiple Inlet Mach Operating Conditions. *Aerospace* **2019**, *6*, 64. [CrossRef]

27. Celik, I.B.; Ghia, U.; Roache, P.J.; Freitas, C.J.; Coleman, H.; Raad, P.E. Procedure for estimation and reporting of uncertainty due to discretization in CFD applications. *J. Fluids Eng. Trans. Asme* **2008**, *130*, 0780011–0780014. [CrossRef]
28. Lee, K.B.; Wilson, M.; Vahdati, M. Effects of Inlet Disturbances on Fan Stability. *J. Eng. Gas Turbines Power* **2018**, *141*, 051014. [CrossRef]
29. Zhang, W.; Vahdati, M. A Parametric Study of the Effects of Inlet Distortion on Fan Aerodynamic Stability. *J. Turbomach.* **2018**, *141*, 011011. [CrossRef]
30. Mohankumar, B.; Hall, C.A.; Wilson, M.J. Fan Aerodynamics With a Short Intake at High Angle of Attack. *J. Turbomach.* **2021**, *143*, 051003. [CrossRef]
31. Benini, E.; Venturelli, G.; Łaniewski Wollk, L. Comparison between pure and surrogate assisted evolutionary algorithms for multiobjective optimization. *Front. Artif. Intell. Appl.* **2016**, *281*, 229–242. [CrossRef]
32. Benini, E. Three-Dimensional Multi-Objective Design Optimization of a Transonic Compressor Rotor. *J. Propuls. Power* **2004**, *20*, 559–565. [CrossRef]
33. Battiston, A.; Magrini, A.; Ponza, R.; Benini, E. Design Optimization of Rear-Fuselage Boundary-Layer Ingestion Shrouded Propulsor. *J. Aircr.* **2025**, *62*, 602–612. [CrossRef]
34. Davis, M.W., Jr.; Cousins, W.T. Evaluating Complex Inlet Distortion With a Parallel Compressor Model: Part 1—Concepts, Theory, Extensions, and Limitations. In Proceedings of the Turbo Expo: Power for Land, Sea, and Air, Vancouver, BC, USA, 6–10 June 2011; Volume 1: Aircraft Engine; Ceramics; Coal, Biomass and Alternative Fuels; Wind Turbine Technology, pp. 1–12. [CrossRef]
35. Davis, M.W., Jr.; Cousins, W.T. Evaluating Complex Inlet Distortion With a Parallel Compressor Model: Part 2—Applications to Complex Patterns. In Proceedings of the Turbo Expo: Power for Land, Sea, and Air, Vancouver, BC, USA, 6–10 June 2011; Volume 1: Aircraft Engine; Ceramics; Coal, Biomass and Alternative Fuels; Wind Turbine Technology, pp. 1–11. [CrossRef]
36. Li, Z.; Zhu, X.; Yan, Z.; Pan, T.; Zheng, X. Numerical study on the Re effects on the tip flow structures of transonic fan under inlet distortion. *Aerosp. Sci. Technol.* **2023**, *141*, 108530. [CrossRef]